Epitaxial growth of Al_9Ir_2 intermetallic compound on Al(100): Mechanism and interface structure

J. Kadok,[1] K. Pussi,[2] S. Šturm,[3,4] B. Ambrožič,[3,5,4] É. Gaudry,[1,4] M.-C. de Weerd,[1,4] V. Fournée,[1,4] and J. Ledieu[1,4,*]

[1]*Institut Jean Lamour, UMR 7198 CNRS - Université de Lorraine, Campus Artem, 2 allée André Guinier, BP 50840, 54011 Nancy Cedex, France*

[2]*LUT School of Engineering Science, Lappeenranta University of Technology, P.O. Box 20, FIN-53851 Lappeenranta, Finland*

[3]*Jožef Stefan Institute, Department for Nanostructured Materials, Ljubljana, Slovenia*

[4]*International Associated Laboratory PACS2, CNRS and Université de Lorraine, Nancy-JSI, Ljubljana, Slovenia*

[5]*Jožef Stefan International Postgraduate School, Jamova cesta 39, SI-1000 Ljubljana, Slovenia*

(Received 22 December 2017; published 25 April 2018)

The adsorption of Ir adatoms on Al(100) has been investigated under various exposures and temperature conditions. The experimental and theoretical results reveal a diffusion of Ir adatoms within the Al(100) surface selvedge already at 300 K. Above 593 K, two domains of a $(\sqrt{5}\times\sqrt{5})R26.6^\circ$ phase are identified by low energy electron diffraction (LEED) and scanning tunneling microscopy measurements. This phase corresponds to the initial growth of an Al_9Ir_2 compound at the Al(100) surface. The Al_9Ir_2 intermetallic domains are terminated by bulklike pure Al layers. The structural stability of $Al_9Ir_2(001)$ grown on Al(100) has been analyzed by density functional theory based calculations. Dynamical LEED analysis is consistent with an Ir adsorption leading to the growth of an Al_9Ir_2 intermetallic compound. We propose that the epitaxial relationship $Al_9Ir_2(001)\|Al(100)$ and $Al_9Ir_2[100]\|Al[031]/[013]$ originates from a matching of Al atomic arrangements present both on Al(100) and on pure Al(001) layers present in the Al_9Ir_2 compound. Finally, the interface between Al_9Ir_2 precipitates and the Al matrix has been characterized by transmission electron microscopy measurements. The cross-sectional observations are consistent with the formation of $Al_9Ir_2(001)$ compounds. These measurements indicate an important Ir diffusion within Al(100) near the surface region. The coherent interface between Al_9Ir_2 and the Al matrix is sharp.

DOI: 10.1103/PhysRevMaterials.2.043405

I. INTRODUCTION

Following successive investigations of the Al-Ir phase diagram [1], different complex metallic alloy phases have been identified within this system. Among them, we will mention the $Al_{2.4}Ir$ [2], the $Al_{28}Ir_9$ [3], and the $Al_{45}Ir_{13}$ [4] compounds with relatively large unit cells. It has been well reported that the structural complexity often inherent to Al-based intermetallic compounds can lead to unique chemical and physical bulk and surface properties [5]. While the bulk structure is still under investigation for several of these complex phases, information regarding the surface structure of Al-Ir compounds is nonexistent. However, Al-Ir intermetallic phases have already attracted much interest in the field of thin-film coating due to their promising properties. Of high melting temperature, Al-Ir phases have been considered as protective coating for instance in gas turbine engines [6]. Here, the protective layer acts also as a barrier against rapid oxidation via the formation of an aluminium oxide scale. Benefiting from the lowest oxygen permeation of Ir among all known materials, Al-Ir phases inhibit diffusion of oxygen towards underlying substrates [6,7]. Hence, Al-Ir based coatings represent new systems with combinatorial properties. However, there is still a need for improved deposition processes. Self-propagating high-temperature synthesis of Ir-Al phases and Al pack cementation are among the methods used to obtain high-quality thick layers of intermetallic compounds [6,8,9,11]. The latter chemical vapor deposition technique has been successfully used to produce a double-layer Ir-Al intermetallic coating on Ir [9]. The oxidation behavior of such coating has been subsequently studied from 1673 K to 2273 K [10]. Pack cementation is also the process chosen to aluminize Ir-based coated superalloys, leading to the formation of Al-Ir based coating [11]. As evidenced with these studies, the interfacial and microstructural evolutions of the material upon the Al-Ir formation and oxidation are complex. These features will dictate in fine the coating physical and chemical properties including adhesion to the substrate, wear, and oxidation resistance.

To understand and somehow tailor these above properties, a detailed knowledge of the interface, bulk, and surface structures are required down to the atomic scale. Regarding the surface structure, one approach consists of studying model surfaces under ultrahigh vacuum which requires large single crystals [12]. Due to difficulties inherent to the phase diagram and to the cost of the Ir element, large enough complex Al-Ir single crystals for surface characterization are not yet available. Consequently, an alternative route had to be chosen to study Al-Ir surface phases. In line with the above synthesis studies, Gall' *et al.* [13] have characterized the Al and Ir element interactions by Al adatom adsorption on an Ir(111) surface under ultrahigh-vacuum conditions (UHV), hence exploring the Ir-rich side of the Ir-Al phase diagram. While a layer-by-layer growth is observed at room temperature, high-temperature deposition (1100 K to 1300 K) results in the formation of

*Corresponding author: julian.ledieu@univ-lorraine.fr

 ©2018 American Physical Society

Ir_4Al surface aluminide [13]. Beyond this temperature range, it was demonstrated that Al desorption occurs via thermal desorption, hence defining the temperature limit above which Ir_4Al decomposes.

As opposed to Al pack cementation where Al is deposited on an Ir-rich surface, a reverse strategy may be more pertinent when an Al-Ir intermetallic film should be formed on an Al-rich substrate. As previously explained, the material would benefit protection against extensive oxidation and an enhanced surface hardness for an improved wear resistance. While Ir deposition via several techniques has been achieved [14,15], reports dealing with Ir adsorption on Al surfaces are still limited [16]. To this end, the adsorbate-substrate system selected here is inverted with respect to the works of Gall' *et al.* [13], focusing on the Al-rich part of the phase diagram. Iridium adatom deposition on Al(100) should result in a greater intermixing length at room temperature [16] and *a fortiori* to the formation of Al-rich Al-Ir phases. Combining both experimental and theoretical methods, the Ir adsorption on the Al(100) surface has been characterized from submonolayer regime deposition up to the formation of micrometer-sized Al-Ir crystallites embedded in the Al matrix. The particular intermetallic to Al(100) interfacial orientations and the sharp interface will be explained based on similar local atomic arrangement decorating the Al(100) surface and being present within bulk layers of the grown Al-Ir compound. The interface structure, the intermetallic phase grown, and the associated surface structure will be determined using experimental and theoretical methods. As mentioned above, these are the first step towards an understanding of the associated Al-Ir physical and chemical properties.

After describing the experimental details in Sec. II, the experimental results will be presented in Sec. III. Then, these initial observations will be completed by a dynamical low energy electron diffraction (LEED) analysis in Sec. IV. From *ab initio* calculations, structural relaxation and segregation energy will be computed for different positions of the Ir atom within the Al(100) region. The results along with an interface model will be described in Sec. V. Finally, the Al-Ir compounds and Al(100) interface will be characterized using transmission electron microscopy (TEM) analysis in Sec. VI. The discussion and conclusions will be presented in Sec. VII.

II. EXPERIMENTAL DETAILS

The experiments have been carried out in a UHV chamber with a base pressure around 5×10^{-11} mbar. The Al(100) surface (extracted from a homegrown Al single crystal) was cleaned before each new deposition by few cycles of Ar^+ sputtering at 2.5 keV followed by 30 min annealing up to 800 K. The iridium (Goodfellow, 99.9%) deposition was carried out with an Omicron EFM3 electron beam evaporator with integrated flux monitor. The pressure of the chamber was kept in the low 10^{-10} mbar range during the deposition. The sample has been characterized using low energy electron diffraction (LEED), x-ray photoelectron spectroscopy (XPS), and scanning tunneling microscopy (STM) measurements. All STM measurements have been carried out at room temperature. The amount of Ir deposited on the surface of the Al(100) sample is given in monolayer equivalent (MLE). As intermixing occurs already at room temperature in the Ir/Al(100) system, the deposition rate of the source has been calibrated on Cu(110) and cross-checked on Ag(111). During their Ir/Cu(100) adsorption experiment, Gilarowski *et al.* [17] calibrated Ir deposition using both XPS and a quartz crystal microbalance. As presented in Fig. 6 in Ref. [17], an Ir_{4f}/Cu_{3p} ratio equal to 1.9 corresponds to a nominal Ir coverage of 1.5 ML at room temperature. A similar adsorption experiment has been performed on a Cu(110) surface at 300 K. Assuming to a first approximation a similar growth mode and correcting for the different atomic surface density between both Cu surfaces, 1 MLE is defined here as the Ir exposure needed to obtain a full monolayer on a Cu(110) surface at room temperature. To verify the deposition, Ir adsorption has been also carried out on a Ag(111) surface held at 693 K. Indeed, Ir and Ag elements are immiscible in the bulk and do not form surface compounds [18].

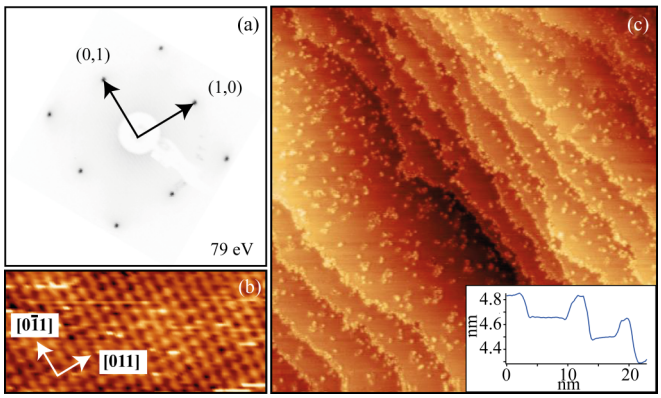

FIG. 1. (a) LEED pattern obtained on the clean Al(100) surface after annealing to 800 K. (b) Atomic resolution STM images (5.7 nm×2.7 nm) of the clean Al(100) surface. (c) 180 nm×180 nm STM image with 0.2 MLE Ir coverage on Al(100) at 300 K ($V_b = 2.4$ V, $I_t = 0.08$ nA). Inset: One-dimensional plot profile across several terraces.

For detailed TEM/STEM studies of the Al_9Ir_2/Al interface in a cross-sectional view, an electron-transparent lamellae was prepared by a modem focused ion beam scanning electron microscope (FIB-SEM; HeliosNanolab 650, FEI, Eindhoven, The Netherlands). The experimental high-angle annular dark-field scanning transmission electron microscopy (HAADF-STEM) images and selected area electron diffraction (SAED) were recorded using a C_s-aberration-corrected probe (JEM-ARM 200CF; JEOL, Tokyo, Japan) operated at 200 keV, with a spatial resolution in STEM mode of 0.08 nm. The collection semiangle for the HAADF detector was set between 45–180 mrad. The elemental composition across the interface was analyzed in the STEM mode of operation by utilizing an electron energy-loss spectrometer (GIF Quantum, Gatan, Pleasantville, USA).

III. IRIDIUM ADSORPTION BETWEEN 300 K AND 693 K

Following the surface preparation described above, a typical LEED pattern obtained from the Al(100) surface is presented in Fig. 1(a). The surface unit cell size ($a = 2.86$ Å) and orientation have been also determined from atomically resolved STM images [Fig. 1(b)]. Upon adsorption of Ir at 300 K, the growth

proceeds with the decoration and roughening of the Al(100) step edges along with the formation of irregularly shaped islands on terraces. As demonstrated later, it is likely that these islands (bright protrusions of 1–3 Å height) correspond to Al atoms originating from a place exchange mechanism with impinging Ir atoms. These Al adatoms increasing with Ir exposure will diffuse to form stable nuclei on terraces and at step edges. A one-dimensional plot profile across several terraces [inset in Fig. 1(c)] reveals an island nucleation on the upper side of the step edges; i.e., the adatoms' diffusion towards lower terraces is inhibited by a large enough Ehrlich-Schwoebel barrier [19,20]. With increasing Ir deposition, a rough and disordered film is formed as evident from the decreasing LEED pattern quality and from STM measurements across terraces. This is in clear contrast with the adsorption of Al adatoms on Ir(111) [13], where a layer-by-layer growth of Al film occurs.

When Ir adsorption is carried out with the Al(100) surface held above 623 K, additional diffraction spots appear on the LEED pattern. The latter is qualitatively similar to the diffraction pattern observed after post-annealing a room-temperature deposited film above 593 K. The sharp diffraction spots circled in Fig. 2(a) originate from two domains of a $(\sqrt{5}\times\sqrt{5})R26.6^\circ$ phase. Both domains are mirror symmetric with respect to the [011] substrate direction, i.e., the a axes of the surface unit cell. The respective intensities of the diffraction spots for both domains appear similar, suggesting an equal amount of the two domains at the surface.

The STM measurements performed under different Ir exposures [Figs. 2(b) and 2(c)] confirm the domain orientations deduced from the LEED analysis. Both domains exhibit a square unit cell with a measured lattice parameter equal to $a = 6.4 \pm 0.3$ Å, i.e., $\sqrt{5}$ times the Al(100) surface unit cell parameters. Atomically high protrusions (bright features) and depressions are always present on such terraces. Figure 2(d) shows another type of surface termination, referred as void-rich terraces, commonly coexisting with those presented in Figs. 2(b) and 2(c). In fact, the void-rich termination can be regarded as an adlayer above the terminations presented in Figs. 2(b) and 2(c) with a step height equal to 2.1 ± 0.1 Å. For several void-rich terraces, the underneath planes have been identified through the largest pores. The domain orientations of these terraces and the lattice parameters [see inset in Fig. 2(d)] are also consistent with two domains of a $(\sqrt{5}\times\sqrt{5})R26.6^\circ$ phase. For the sake of completeness, we will mention another structure which has been occasionally observed on small islands across terraces (not appearing in the LEED patterns). Due to the orientation and its unit cell parameters [$a = 12.8(2)$ Å], it is interpreted as a (2×2) reconstruction if the reference substrate is considered as the $(\sqrt{5}\times\sqrt{5})R26.6^\circ$ domain.

We now turn into the XPS measurements performed after various Ir exposures between 300 K and 693 K. The Ir concentrations measured at the surface are around 19 at.% and 6–7 at.% for 2 MLE deposition at 300 K and 693 K, respectively. While these results clearly indicate an increasing Ir diffusion into the bulk with temperature, the interpretation of the concentration with respect to the phase formed is not straightforward. Indeed, STM observations indicate a nonuniform Ir concentration across surface regions. For instance,

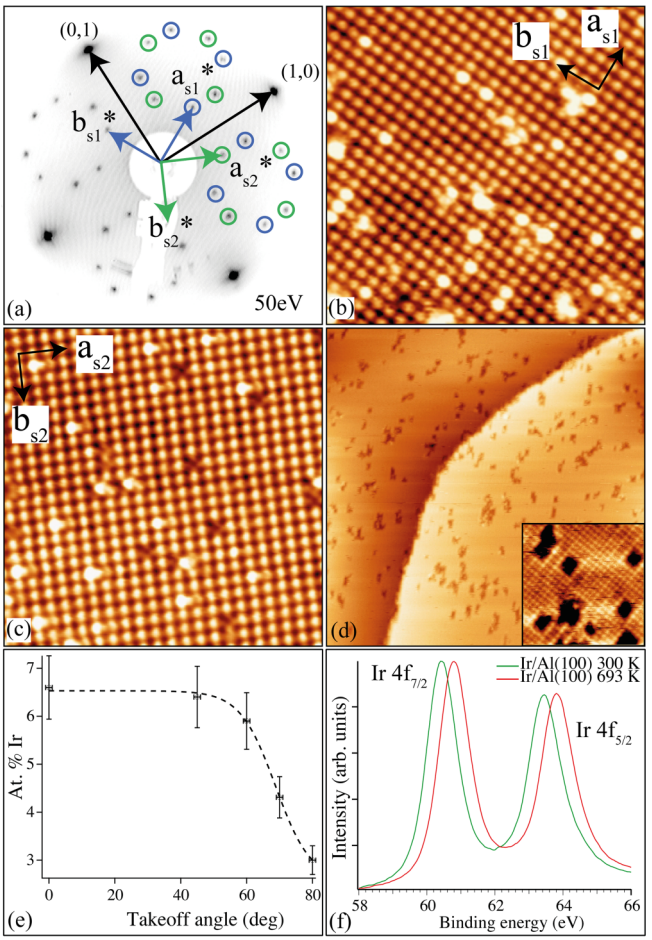

FIG. 2. (a) LEED pattern obtained after dosing 2 MLE Ir on the Al(100) surface held at 640 K. (b), (c) High-resolution STM images (14 nm×14 nm) presenting the two domain orientations of the Al-Ir $(\sqrt{5}\times\sqrt{5})R26.6^\circ$ phase for 2 MLE (b) and 0.7 MLE (c) Ir adsorption, respectively. (d) 100 nm×100 nm STM image with 2 MLE Ir deposition on Al(100) at 693 K. Inset: Higher magnification (14 nm×14 nm) STM image revealing a square unit mesh with $a = 6.4$ Å. (e) At.% of Ir calculated as a function of the XPS takeoff angle. The horizontal and vertical error bars represent the uncertainty originating from the measurements and fits of the XPS spectra, respectively (the dashed line is a guide for the eye). (f) Normalized Ir $4f$ core level spectra after 2 MLE Ir deposition at 300 K and 693 K.

apparently clean Al(100) terraces (characterized by fuzzy steps) have been observed next to Al-Ir domains. Hence, the Al-Ir $(\sqrt{5}\times\sqrt{5})R26.6^\circ$ phase may have a higher Ir content than probed by XPS measurements, a technique averaging laterally over several mm^2. The Ir diffusion into the bulk is further confirmed by angle-resolved XPS measurements. As the measurements get more surface sensitive [high takeoff angle in Fig. 2(e)], there is a clear decrease of the Ir concentration. Then, the Al-Ir $(\sqrt{5}\times\sqrt{5})R26.6^\circ$ phase is clearly Al-rich with a reduced Ir atomic content within the topmost surface layers.

Regarding the core level spectra, their binding energy and overall shape can also provide information about the local bonding environment of the elements. In Fig. 2(f), the Ir $4f$ core level spectra are presented for Ir dosage at room

temperature and 693 K. There is a clear chemical shift of approximately 0.4 eV between the peaks of the two experiments. Similarly, a shift of 0.2–0.3 eV toward lower binding energy is measured for the Al $2p$ peak of the sample after Ir deposition at room-temperature (not shown here). At higher temperature, the Al $2p$ core level spectra are comparable in binding energy and shape to those obtained on the clean Al(100) surface prior to dosing. These results are in agreement with the STM observations showing different atomic arrangements (different Al/Ir interactions) for the two temperature regimes.

After a careful inspection of the known Al-Ir binary phases, the Al_9Ir_2 compound (Pearson symbol $mP22$) appears as the only intermetallic with lattice parameters matching those of the $(\sqrt{5}\times\sqrt{5})R26.6^\circ$ phase. The lattice parameters of the Al_9Ir_2 compound are $a = 6.378(1)$ Å, $b = 6.430(1)$ Å, $c = 8.732(2)$ Å, and $\beta = 94.77(2)^\circ$. The Al_9Ir_2 intermetallic is the most Al-rich compound of all Al-Ir binaries. Hence, the initial growth of this compound would be consistent with the phase diagram since experimentally a small amount of Ir is deposited on a large excess of Al.

IV. DYNAMICAL LEED $I(V)$ ANALYSIS

To further examine the structure of the $(\sqrt{5}\times\sqrt{5})R26.6^\circ$ phase, dynamical LEED analysis has been carried out on the sample after a deposition of 2 MLE of Ir at 693 K. LEED patterns have been acquired for a total energy range of 1700 eV with the sample held at 120 K. For this task, the SATLEED program package [21] was used and the relativistic phase shifts were calculated using the phase shift program [22] that is packaged with SATLEED. The agreement between the theory and the experiment was tested using the Pendry reliability factor (R_P) [23]. A wide range of different model structures has been considered. The intensities of 16 Al(100) spots were extracted as a function of the energy as well as 28 spots from the two $(\sqrt{5}\times\sqrt{5})R26.6^\circ$ domains. As a first observation, spots from the two different domains lead to similar $I(V)$ curves, confirming that these two domains are totally equivalent. All the equivalent curves were summed, averaged, and normalized. This resulted in 8 averaged curves, 4 for Al(100) [index of the spots (10), (11), (20), (21)] and 4 for the two domains [index $(\frac{2}{5}\ \frac{1}{5})$, $(\frac{1}{5}\ \frac{3}{5})$, $(\frac{2}{5}\ \frac{4}{5})$, $(\frac{4}{5}\ \frac{3}{5})$].

To analyze the structure of the $(\sqrt{5}\times\sqrt{5})R26.6^\circ$ phase, the LEED $I(V)$ spectra have been modeled following two approaches. The first set of model structures was based on isolated Ir atoms located at the surface or within bulk planes of the Al(100) substrate. Thus, models have been calculated for Ir adatoms positioned at atop, hollow, and bridge surface sites. Then, substituting one or more Al atoms with Ir has been considered within the topmost, second, third, and fourth layers and also different combinations of these substitutions were tried. Disordered Ir on different layers or combinations of layers using the "average transfer matrix approximation" (ATA) [24] was also considered. The best Al(100)-based structure is obtained for Ir substitution into the second layer, giving $R_P = 0.26$ (model 1).

The second set of model structures was based on the Al_9Ir_2 compound. Different thicknesses and terminations of the slab, both supported by Al(100) and pure Al_9Ir_2 structure, were considered. The best structure from these models was 6 layers of Al_9Ir_2 on top of Al(100) giving $R_P = 0.29$ (model 2).

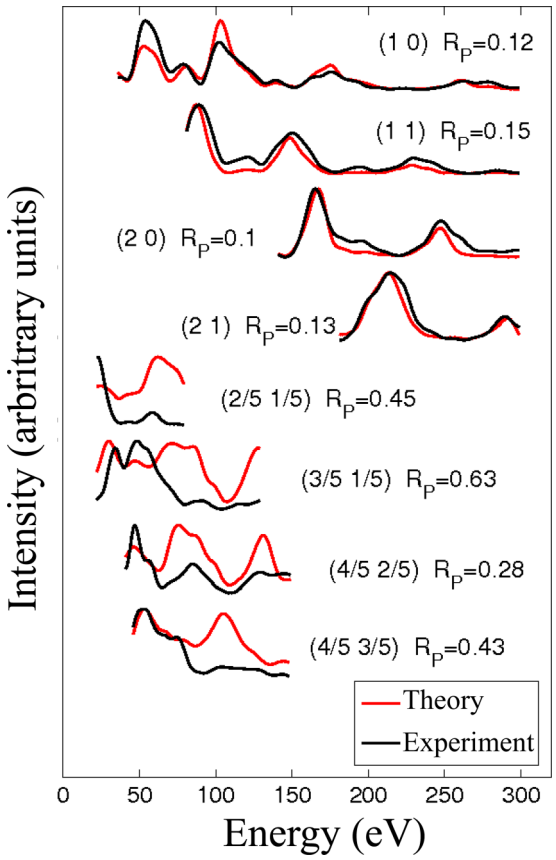

FIG. 3. Experimental and calculated LEED $I(V)$ spectra collected on the Al-Ir $(\sqrt{5}\times\sqrt{5})R26.6^\circ$ phase held at 120 K.

While the individual model leads to acceptable R_P values and a reasonable agreement with the experimental $I(V)$ curve, mixing both models gives $R_P = 0.23$ (see Fig. 3). This reduced Pendry R factor has been obtained for a 40:60 mixture of both models (model 1: model 2). This suggests that the LEED $I(V)$ measurements should be considered as a snapshot representing different stages of Ir diffusion towards the formation of the Al_9Ir_2 compound.

V. *AB INITIO* CALCULATIONS

A. Computational details

Due to the complexity of the system, *ab initio* calculations have been carried out to gain more insights into the structural stability, the segregation energy, and the possible Al-Ir/Al interfacial model. The calculations based on density functional theory (DFT) are performed with the Vienna simulation package (VASP) [25–28]. The interaction between the valence electrons and the ionic core is described using the projector-augmented wave (PAW) method [29,30] and the calculations are performed within the generalized gradient approximation (GGA-PBE) [31,32]. Spin polarization is considered. A plane wave basis set for the electron wave function with a cutoff energy of 450 eV is used. Integrations in the Brillouin zone are performed using a $13\times13\times1$ k grid generated according

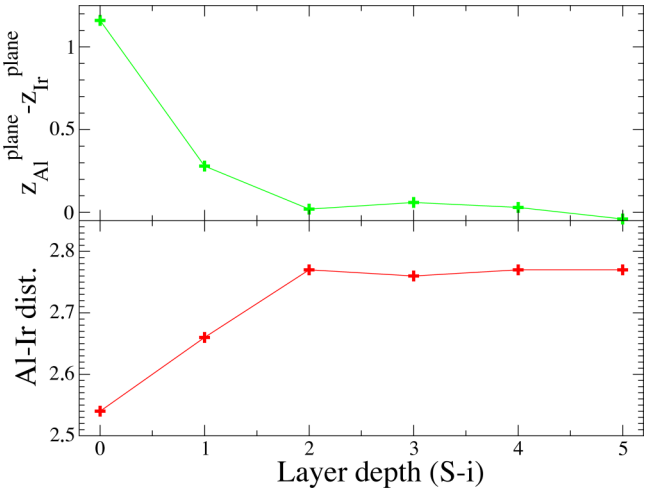

FIG. 4. Structural relaxations obtained by burying an iridium atom into an Al(100) crystal. The smallest Al-Ir distances and the quantity $(z_{Al^{plane}} - z_{Ir^{plane}})$ are given in Å. The x coordinate shows the Ir position in the slab: 0 for surface layer (S), 1 for subsurface layer (S-1), etc.

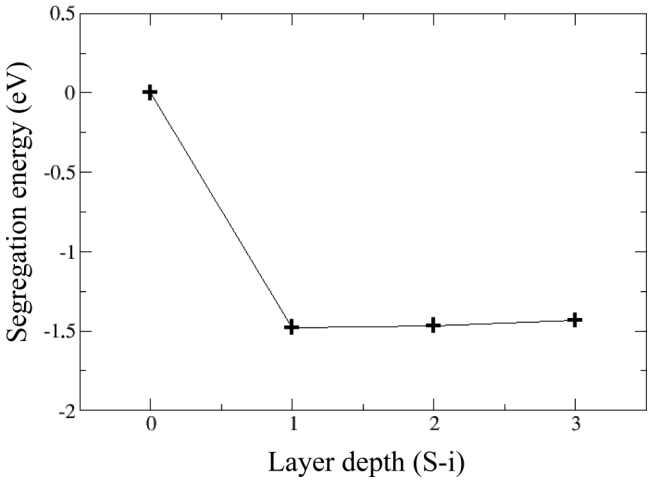

FIG. 5. Segregation energy (eV) evaluated for nonrelaxed slabs. The energy of the slab containing a surface Ir atom is taken as the reference energy. The x coordinate shows the Ir position in the slab: 0 for surface layer (S), 1 for subsurface layer (S-1), etc.

to the Monkhorst-Pack scheme. Structures are relaxed using a conjugate-gradient algorithm until the atomic forces are less than 0.02 eV/Å. The aluminium bulk cell parameter (4.04 Å) obtained by the calculations is in excellent agreement with the reported experimental data (4.05 Å) [33].

In the following, two different approaches have been undertaken. First, the segregation of the Ir atom in Al(100) was studied systematically by burying the Ir atom (in substitution of an Al atom) into Al(100). In a second step, the possibility to form an Al-Ir surface alloy on Al(100) was investigated by burying one (001) atomic plane of the Al_9Ir_2 phase into the Al(100) surface region. In both cases, we used a slab consisting of 19 layers: 7 layers fixed at the bottom and 12 layers allowed to relax. The calculated Al bulk structure has been used to build the interface model. Here, a commensurate interface is required between $Al_9Ir_2(001)$ and Al(100) bulk planes. In agreement with the experimental observations, a $(\sqrt{5}\times\sqrt{5})R26.6^\circ$ surface unit cell has been considered for fcc Al ($\sqrt{5}\times a/\sqrt{2} = 6.39$ Å). This leads to a square surface unit cell with a lattice mismatch smaller than 1%.

B. Structural relaxation

The presence of a surface Ir atom is unlikely. This is the result emerging from the structural relaxations performed for different Ir adatom positions within the Al(100) surface selvedge. Indeed, the relaxations of the slab containing a surface Ir atom are large, leading to the displacement of the Ir atom well below the Al surface termination (1.16 Å below). The relaxations are much smaller when the Ir atom is positioned in the subsurface layer. Even in this case, the transition metal atom lies after relaxation below the Al subsurface layer (0.28 Å). Structural relaxations become negligible when the Ir atom is located in the S-2 layer, or deeper in the crystal (see Fig. 4). The Al-Ir distances are then equal to 2.77 Å (see Fig. 4), being roughly equal to the sum of the atomic radii of the elements ($r_{Al} = 143$ pm and $r_{Ir} = 136$ pm). Figure 4 (right panel) shows the difference between the z coordinate of the Ir atom and the Al plane in the considered slab. A minimum is already reached once Ir atoms are in the S-2 layer, i.e., they remain within the Al plane.

C. Segregation energy

Since the atomic relaxations do not necessarily keep the layer-by-layer structure, we have evaluated the nonrelaxed segregation energy (atoms fixed at their initial position). The results are plotted in Fig. 5. Once more, this indicates that the presence of surface Ir atoms is very unlikely. Energy differences for slabs containing Ir atoms at subsurface planes, or deeper in the crystal, are similar. The energy difference between a slab containing a surface or subsurface Ir atom is 1.48 eV.

D. Ir deposition on Al(100): Construction of an interface model

As demonstrated by the experimental results, the formation of a surface alloy is expected upon adsorption of Ir at high temperature. The Al-Ir intermetallic compound which contains the lowest Ir amount is Al_9Ir_2. Therefore, in the following part, we investigate the possibility of growing the Al_9Ir_2 compound on Al(100).

The Al_9Ir_2 crystallizes in the $P2_1/c$ space group, with the following parameters: $a_{Al_9Ir_2} = 6.38$ Å, $b_{Al_9Ir_2} = 6.43$ Å, $c_{Al_9Ir_2} = 8.73$ Å, and $\beta_{Al_9Ir_2} = 94.77^\circ$. The Al_9Ir_2 intermetallic compound can be described as a layered compound. Its structure is built by the stacking of two atomic layers that alternates roughly perpendicular to the z axis [see Fig. 10(a)]: a pure and slightly rumpled Al atomic layer (F type) made of 5 Al atoms, and a highly puckered layer (P type) made of 4 Al and 2 Ir atoms.

In order to build a structural model, a commensurate interface must be constructed between $Al_9Ir_2(001)$ and Al(100) bulk planes. Considering a $(\sqrt{5}\times\sqrt{5})R26.6^\circ$ surface unit cell for fcc Al, i.e., a square surface unit cell of parameter

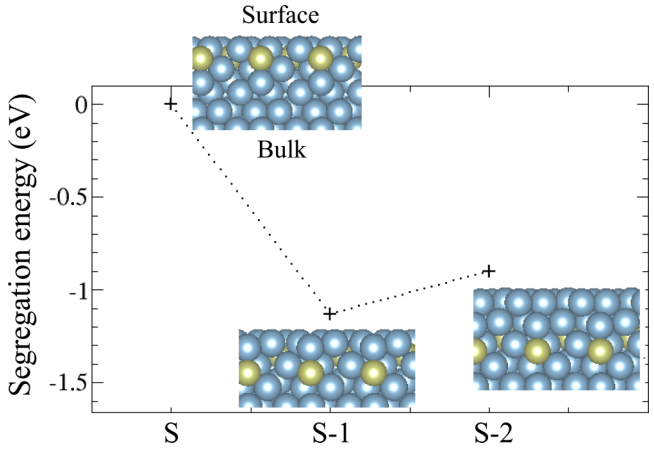

FIG. 6. Segregation energy (eV) evaluated when burying the P-type layer in the 19-layer-thick Al(100) slab. The energy of the system containing a P type as the surface layer is taken as the reference energy.

$a_{(\sqrt{5}\times\sqrt{5})R26.6^\circ} = 6.39$ Å, leads to a lattice mismatch smaller than 1%.

In the following, a P-type layer is buried in the $(\sqrt{5}\times\sqrt{5})R26.6^\circ$ Al(100) slab. The segregation energy is evaluated as a function of the depth. Results are gathered in Fig. 6. The segregation energy is in the range 0.9–1.1 eV, i.e., of the same order of magnitude as Ir in Al(100). Hence, the Al_9Ir_2 puckered layer is not favored as a surface termination from energetics.

VI. INTERFACE CHARACTERIZATION

The aim of the TEM study was to determine the compositional variations and the local atomic configuration at the Al_9Ir_2/Al interface, mainly focused to the last layer of the Al substrate and the first layer of the Al_9Ir_2 film. Conventional TEM and SAED analysis of the interface region in a cross-sectional view is shown in Fig. 7, revealing the formation of

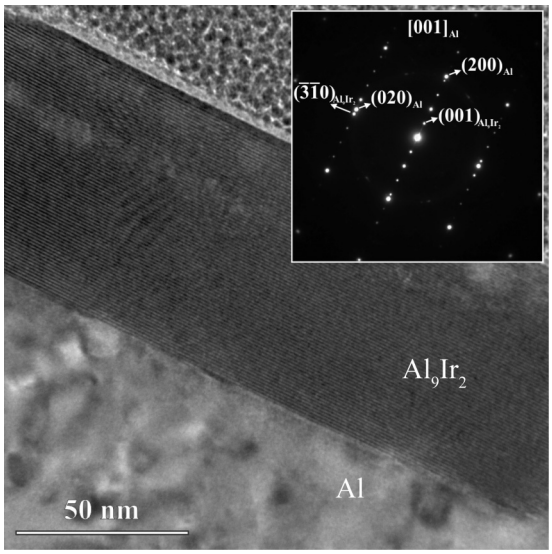

FIG. 7. TEM image of Al_9Ir_2 film grown on Al substrate with the corresponding SAED pattern acquired from the interface region.

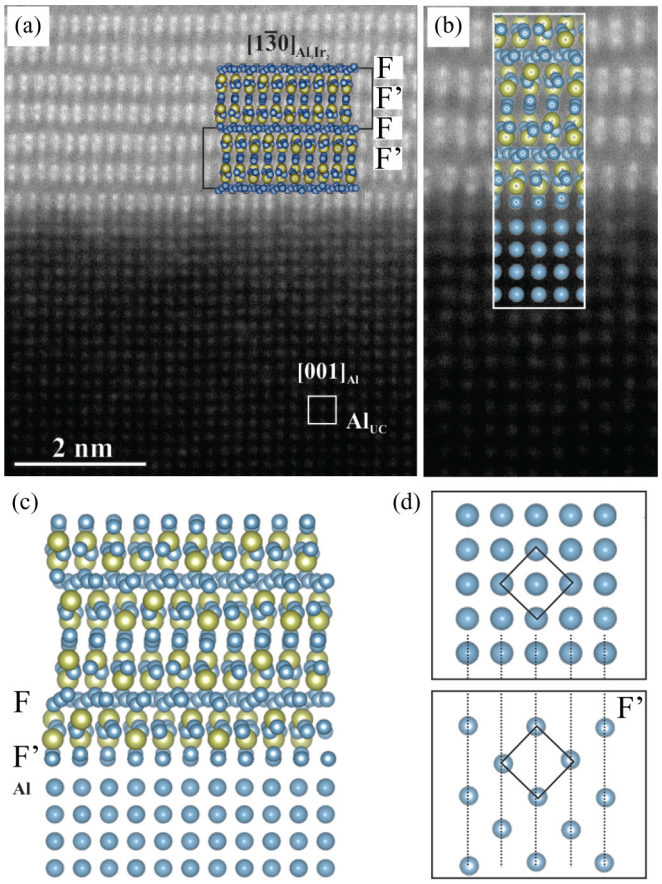

FIG. 8. (a) Atomically resolved HAADF-STEM image of the interface region with the superimposed structural units of Al_9Ir_2 viewed in $[1\bar{3}0]_{Al_9Ir_2}$ projection. (b) Enlarged image with the (c) superimposed atomic model of the interface region between the Al substrate and Al_9Ir_2 phase. (d) The representative Al substrate termination plane and first Al-rich atomic layer in Al_9Ir_2 film (F′) viewed perpendicular to the interface.

70-nm-thick Al_9Ir_2 film on the Al substrate. The corresponding SAED pattern of the interface region was acquired in the $[001]_{Al}$ zone-axis orientation. The diffraction pattern exhibits a superposition of the Al substrate and Al_9Ir_2 film zone-axis patterns, indicating that the $(100)_{Al}$ lattice planes are parallel with $(001)_{Al_9Ir_2}$. On the other hand, the diffraction spots $(020)_{Al}$ and the $(\bar{3}\bar{1}0)_{Al_9Ir_2}$ are only partially coinciding, which originates from the small tilt of 4.6° between the substrate and the film set of planes, respectively. The theoretical lattice mismatch between Al and Al_9Ir_2 in this direction is 0.5%, which is in agreement with the experimental SAED pattern. The orientation relationship between the Al substrate and Al_9Ir_2 film for one domain deduced from the experimental SAED pattern can be described by the following relation: $(100)_{Al}\,[001]_{Al} \parallel (001)_{Al_9Ir_2}\,[1\bar{3}0]_{Al_9Ir_2}$.

A representative atomic-resolution HAADF-STEM image (often refered as a Z-contrast image) of the interface region in the $[001]_{Al}$ zone axis is shown in Fig. 8(a). The contrast variation in the atomic-resolution Z-contrast images roughly follows the Z^2 dependence on the average atomic number of the probed atom column. Consequently, the intensity of HAADF-STEM images reflects compositional variations at

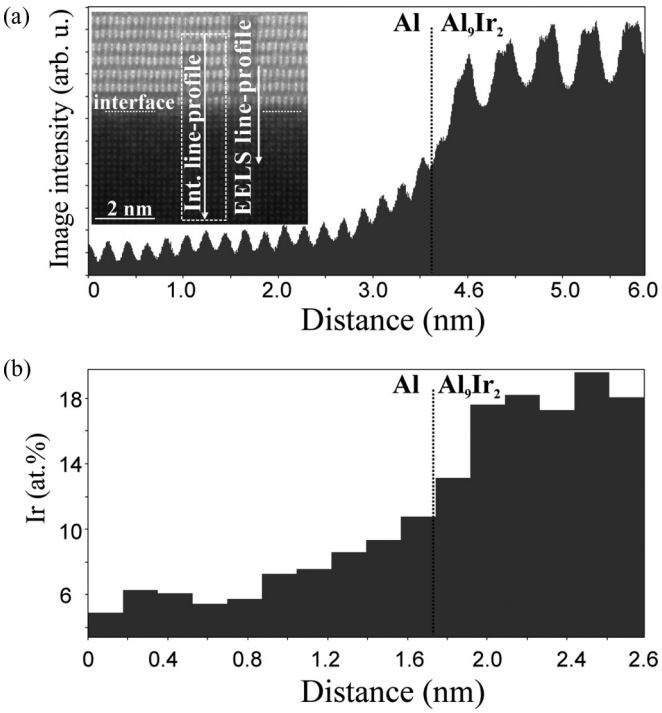

FIG. 9. (a) HAADF-STEM intensity and (b) compositional profiles perpendicular to the Al/Al_9Ir_2 interface.

the atomic scale, which makes the reconstruction of both atomic arrangements and atoms types at an interface relatively straightforward. The substrate Al columns viewed along the $[001]_{Al}$ zone axis are represented by a squarelike pattern of discrete dots [the unit cell is marked in Fig. 8(a)]. The interface region in the area of observation is atomically flat. The Al_9Ir_2 film viewed in the $[1\bar{3}0]_{Al_9Ir_2}$ zone axis can be described as a periodic stacking of unit structure blocks, moved by a translation vector of $\frac{1}{2}[\bar{3}\bar{1}0]_{Al_9Ir_2}$, where the glide plane is characterized by a puckered Al dense plane (F). In a given viewing projection the unit structure block is defined by two pairs of partly overlapping Ir and Al columns. The atomic arrangement between two sets of Ir(Al)-rich regions is defined by a highly directional, $[001]_{Al_9Ir_2}$, densely packed set of three Al columns (F′). In the HAADF-STEM image only the dumbbells of the Ir(Al)-rich columns are clearly visible. The weak and blurred background contrast in the F-plane regions is related to both lower atomic number of Al(13) when compared with Ir(77) and small projected distance between neighboring Al columns, beyond the given spatial resolution of the electron probe. The region marked by F′ is signified by a weak striplike contrast connecting the neighboring bright Ir-rich dumbbells.

Figure 8(b) shows the reconstructed local atomic structure of the Al_9Ir_2/Al interface superimposed on experimental HAADF-STEM image, viewed on the $[001]_{Al}$ zone axis. The structural model, shown in Fig. 8(c), was deduced based on the observed stacking sequence of the Al_9Ir_2 film and contrast variations at the interface region. The representative Al-rich atomic layers in the Al substrate (Al) and in the Al_9Ir_2 film (F′) viewed perpendicular to the interface are shown in Fig. 8(d). In the given atomic configuration the best match of the model to the experimental image is obtained when the first Al layer of the Al_9Ir_2 film is in the F′-type configuration.

Another interesting observation in the experimental HAADF-STEM images is related to the nonuniform contrast in the Al substrate region, which appears brighter close to the interface. This phenomenon is more clearly presented by a 5.8 nm long line profile, which is averaged over the width of 1.5 nm perpendicular to the interface, as shown in Fig. 9(a). The steady decrease of the background intensity from the interface into the substrate can be explained by partial accommodation of Ir atoms in the Al matrix. To unequivocally determine the Ir diffusion profile into the Al substrate, a quantitative compositional point-by-point analysis was performed across the interface by utilizing quantitative EELS analysis, and using Al-K and Ir-$M_{4,5}$ ionization edges, respectively. Analytical spatial resolution was set to 0.17 nm. As shown in Fig. 9(b), the compositional profile extending from the Al_9Ir_2 film into the Al substrate clearly confirms the diffusion of Ir from the surface approximately 1.5 nm deep into the Al substrate matrix.

VII. DISCUSSION AND CONCLUSIONS

Following the work of Buchanan *et al.* [16], a greater intermixing length was expected for Ir adsorption on Al(100) compared to the Al/Ir(111) system. Indeed, an intermixing length of 54 Å has been measured for Ir deposited on an Al sample at room temperature. Moreover, considering the elemental surface energies of both Al (1.1 J m^{-2}) and Ir (3.0 J m^{-2}) [34], it is energetically more favorable to have Ir embedded in the Al surface. Consequently, the disordered terraces observed in Fig. 1(c) are likely Al-rich features originating from a place exchange mechanism. Such growth mode has already been reported for the Ir/Cu(100) system, even though the Ir-Cu phase diagram suffers from a wide bulk miscibility gap.

The Al-Ir $(\sqrt{5}\times\sqrt{5})R26.6^\circ$ phase has been systematically observed above 593 K and was found to be stable up to 800 K [preparation temperature for Al(100)]. Combining the different results presented above, the formation of the $(\sqrt{5}\times\sqrt{5})R26.6^\circ$ phase corresponds to the onset of the formation of the Al_9Ir_2 compound. An important Ir diffusion within the Al(100) surface selvedge is expected at this relatively high temperature and it would be consistent with the repeated cleaning cycles (7–10 preparations) needed to remove Ir from Al(100) near-surface region.

As depicted in Fig. 10(a), the Al_9Ir_2 compound can be described as a periodic stacking of F- and P-type atomic layers along the [001] direction. The in-plane structure of F and F′ layers can be described as slightly distorted square arrangements of Al atoms [see Fig. 10(b)]. Indeed, the closest interatomic Al-Al distances range between 2.78 Å and 2.86 Å. Hence, F/F′ layers can be approximated as "Al(100)-like" planes with a still greater rumpling compared to the Al(100) plane, the latter being presented in Fig. 10(b) (right). Due to the symmetry of the crystal structure ($P2_1/c$ space group), the F and F′ planes are related to each other by a 2_1 screw axis along b or by a glide operation along the c axis. The Al squares are rotated by $\pm 26.5^\circ \pm 0.5^\circ$ from the Al_9Ir_2 [100] unit

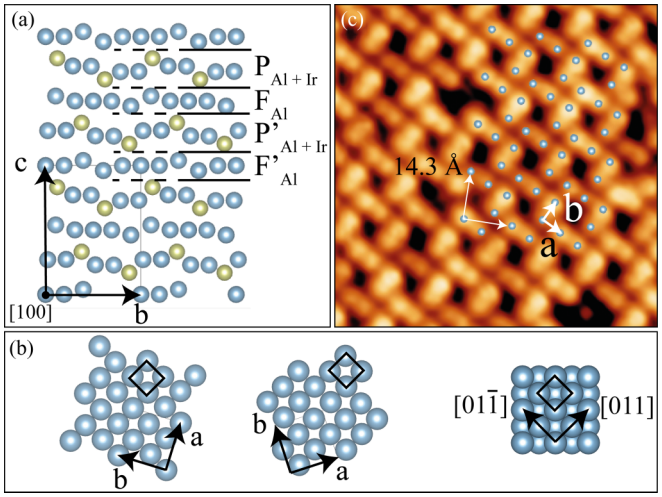

FIG. 10. (a) Representation of the Al_9Ir_2 crystal structure as a sequence of Al flat (F) and Al+Ir puckered (P) layers along the c axis. The angle between c and a axes is 94.78°. (b) Left and middle panels: Visualization of two consecutive pure Al planes along the c axis. Their atomic arrangement consists of small irregular Al squares, which have dimensions similar to the unit cell of the Al(100) surface (right). To match the Al(100) unit cell orientation, the two pure Al layers have been rotated by ±26.6°. (c) 9 nm×9 nm high-resolution STM image revealing an additional structure observed across terraces. An incomplete pure Al layer has been superimposed on the high-resolution STM image (5 nm×5 nm) to describe the local structure. The image has been collected on a second Al(100) sample mounted with a different orientation compared to Figs. 2(a) and 2(b).

cell direction. This rotation is key to understanding the origin of the $(\sqrt{5}\times\sqrt{5})R26.6°$ phase. At the $Al_9Ir_2(001)$/Al(100) interface, the common Al plane can be either of F or F′ type. Hence, the alignment of the Al square motifs present in F and F′ with the Al(100) surface unit cell leads to two possible orientations of the Al_9Ir_2 unit cell. The latter are then orientated at ±26.6° from the substrate [011] direction [see Fig. 10(b)]. In reciprocal space, each unit cell orientation will generate a mirror-symmetric domain with respect to the substrate [011] direction. Due to the symmetry that relates F/F′ players, these domains are indistinguishable in the LEED pattern with a coincidence of the diffraction spots. The LEED pattern is then described using two lattices as in Fig. 2(a).

For large enough domains where terraces have developed, step heights of about half the c^* lattice parameter [where $c^* = c\cos(4.77°)$] have been measured. Due to energetics, it has been established that the Al_9Ir_2 domains terminate at the pure Al bulk layer (F and/or F′). Ignoring the bright defects, the highest contrasts distinguishable in Figs. 2(b) and 2(c) are likely to reflect the subsurface Ir positions. These observations are consistent with previous surface studies performed on intermetallic compounds [35]. Indeed, the investigation of the $Al_9Co_2(001)$ surface, compound isostructural to the Al_9Ir_2 intermetallic, has demonstrated that pure Al layers are preferentially selected as surface terminations. This specific plane selection leads to a single step height across terraces equal to $c^*/2$ [36].

Finally, the STM image in Fig. 2(d) is interpreted as an additional Al layer atop an F-type Al_9Ir_2 plane. As demonstrated by *ab initio* calculations, this corresponds to an S-2 configuration (see Fig. 6), which is energetically less favored by 240 meV than an F-type terminated domain (S-1). This could explain the development of void-rich terraces (the hole density being region and preparation dependent) to finally expose an S-1-like configuration.

For low Ir deposition, a 14.3 Å unit cell structure [Fig. 10(c)] has been identified along with the $(\sqrt{5}\times\sqrt{5})R26.6°$ phase. Two domain orientations of this 14.3 Å phase have also being identified across the surface. Once more, the scarcity of such atomic structures across terraces leads to an absence of additional diffraction spots in the LEED pattern. The structure has been found to coexist with almost clean Al(100) terraces. These results further confirm a certain degree of chemical variation across terraces which makes XPS measurements difficult to rely on. Nevertheless, Fig. 10(c) demonstrates that the 14.3 Å unit cell structure could be related to an incomplete F-type Al_9Ir_2 plane. The domain presented in Fig. 10(c) can be viewed as a $(\sqrt{5}\times\sqrt{5})R26.6°$ reconstruction of the Al-terminated $Al_9Ir_2(001)$ surface itself.

Finally, the coherent growth of the Al_9Ir_2 compound within Al(100) has been clearly demonstrated by cross-sectional TEM measurements. The interface between precipitates and the Al matrix is sharp and its orientation is consistent with the surface observations. The lattice mismatches between Al(100) and $Al_9Ir_2(001)$ in the reported orientation are equal to 0.39% and 0.42% along the [100] and [010] directions of the intermetallic. From these very low values, the strain at the interface should be low which probably explains the absence of dislocations in our measurements. We foresee that Co adsorption on the Al(100) surface under similar conditions should lead to the formation of the (001)-oriented isostructural Al_9Co_2 compound [37]. However, it is likely that the interface structure will differ from a higher lattice mismatch with the Al(100) template (up to 2.9% in the Al_9Co_2 [100] direction). To conclude, our approach has been successful in growing an Al-Ir compound and characterizing its surface structure. Further works will now be undertaken to determine the associated mechanical properties of the Al_9Ir_2-oriented crystallites.

ACKNOWLEDGMENTS

This work was supported by the HPC resources of the IDRIS under the allocation 99642 made by GENCI and by the Academy of Finland through Grant No. 277829. The INC CNRS and the Région Lorraine are acknowledged for funding. This work is a result of cooperation within the European C-MAC and within the French-Slovene collaboration established under Push-Pull Alloys and Complex Compounds (PACS2) Joint Open Laboratory. For the quantitative LEED calculation, the Finnish Grid and Cloud Infrastructure (FGCI) was utilized. High-performance computing resources were partially provided by the EXPLOR center hosted by the University of Lorraine.

[1] H. Okamoto, J. Phase Equilib. Diffus. **30**, 206 (2009).
[2] J. Kadok *et al.* (unpublished).
[3] S. Katrych, V. Gramlich, and W. Steurer, J. Alloys Compd. **407**, 132 (2006).
[4] M. Boström, R. Niewa, Y. Prots, and Y. Grin, J. Solid State Chem. **178**, 339 (2005).
[5] J.-M. Dubois, Chem. Soc. Rev. **41**, 6760 (2012).
[6] R. Darolia, US Patent 6,630,250, B1, Oct. 7, 2003.
[7] H. Hosoda, in *Nanomaterials: From Research to Applications*, edited by H. Hosono, Y. Mishima, H. Takezoe, and K. J. D. MacKenzie (Elsevier, Oxford, 2006), p. 419.
[8] M. Ode, H. Murakami, and H. Onodera, Scr. Mater. **52**, 1057 (2005).
[9] L. Zhu, S. Bai, H. Zhang, Y. Ye, and W. Gao, Surf. Coat. Technol. **258**, 524 (2014).
[10] L. Zhu, G. Du, S. Bai, H. Zhang, Y. Ye, and Y. Ai, Corr. Sci. **123**, 328 (2017).
[11] H. Ehrenreich and L. M. Schwartz, in *Superalloys 2004: Proceedings of the 10th International Symposium on Superalloys*, edited by K. A. Green, T. M. Pollock, H. Harada, T. E. Howson, R. C. Reed, J. J. Schirra, and S. Walston (The Minerals, Metals, and Materials Society, Pittsburgh, PA, 2004), p. 589.
[12] J. Ledieu, É. Gaudry, L. N. S. Loli, S. A. Alarcón, M.-C. de Weerd, M. Hahne, P. Gille, Y. Grin, J.-M. Dubois, and V. Fournée, Phys. Rev. Lett. **110**, 076102 (2013).
[13] N. R. Gall', E. V. Rut'kov, and A. Ya. Tontegode, Phys. Solid State **48**, 369 (2006).
[14] Y. Gong, C. Wang, Q. Shen, and L. Zhang, Vacuum **82**, 594 (2008).
[15] C.-P. Yeh, M. Lisker, J. Bläsing, O. Khorkhordin, B. Kalkofen, and E. P. Burte, Chem. Vap. Deposit. **21**, 46 (2015).
[16] J. D. R. Buchanan, T. P. A. Hase, B. K. Tanner, P. J. Chen, L. Gan, C. J. Powell, and W. F. Egelhoff, Phys. Rev. B **66**, 104427 (2002).
[17] G. Gilarowski and H. Niehus, Surf. Sci. **436**, 107 (1999).
[18] N. R. Gall', E. V. Rut'kov, and A. Ya. Tontegode, Phys. Solid State **46**, 371 (2004).
[19] G. Ehrlich and F. G. Hudda, J. Chem. Phys. **44**, 1039 (1966).
[20] R. L. Schwoebel, J. Appl. Phys. **37**, 3682 (1966).
[21] M. A. Van Hove, W. Moritz, H. Over, P. J. Rous, A. Wander, A. Barbieri, N. Materer, U. Starke, and G. A. Somorjai, Surf. Sci. Rep. **19**, 191 (1993).
[22] A. Barbieri and M. A. Van Hove (private communication).
[23] J. B. Pendry, J. Phys. C **13**, 937 (1980).
[24] H. Ehrenreich and L. M. Schwartz, in *Solid State Physics*, edited by H. Ehrenreich, F. Seitz, and D. Turnbull (Academic Press, New York, 1976).
[25] G. Kresse and J. Hafner, Phys. Rev. B **47**, 558 (1993).
[26] G. Kresse and J. Hafner, Phys. Rev. B **49**, 14251 (1994).
[27] G. Kresse and J. Furthmüller, J. Comput. Mater. Sci. **6**, 15 (1996).
[28] G. Kresse and J. Furthmüller, Phys. Rev. B **54**, 11169 (1996).
[29] P. E. Blöchl, Phys. Rev. B **50**, 17953 (1994).
[30] G. Kresse and D. Joubert, Phys. Rev. B **59**, 1758 (1999).
[31] J. P. Perdew, K. Burke, and M. Ernzerhof, Phys. Rev. Lett. **77**, 3865 (1996).
[32] J. P. Perdew, K. Burke, and M. Ernzerhof, Phys. Rev. Lett. **78**, 1396 (1997).
[33] A. S. Cooper, Acta Crystallogr. **15**, 578 (1962).
[34] L. Vitos, A. V. Ruban, H. L. Skriver, and J. Kollár, Surf. Sci. **411**, 186 (1998).
[35] J. Ledieu, E. Gaudry, and V. Fournée, Sci. Technol. Adv. Mater. **15**, 034802 (2014).
[36] S. Alarcón-Villaseca, J. Ledieu, L. Serkovic-Loli, M.-C. de Weerd, P. Gille, V. Fournée, J.-M. Dubois, and É. Gaudry, J. Phys. Chem. C **115**, 14922 (2011).
[37] M. Boström, H. Rosner, Y. Prots, U. Burkhardt, and Y. Grin, Z. Anorg. Allg. Chem. **631**, 534 (2005).